Journal of Manufacturing Processes 87 (2023) 25–35

Contents lists available at ScienceDirect

Journal of Manufacturing Processes

journal homepage: www.elsevier.com/locate/manpro

Influence of oxygen on performance of multi-principal element alloy as braze filler for Ni-base alloys

Benjamin Schneiderman [a], Alexander Hansen [a], Andrew Chihpin Chuang [b], Zhenzhen Yu [a,*]

[a] Colorado School of Mines, Golden, CO, United States of America
[b] Advanced Photon Source, Argonne National Laboratory, Lemont, IL, United States of America

ARTICLE INFO

Keywords:
Multi principal element alloy
High entropy alloy
Oxygen contamination
Brazing
Ni-base superalloy
High temperature

ABSTRACT

In manufacturing of multi-principal element alloys (MPEAs), the casting process is often a primary point of oxygen introduction to the material system, which was demonstrated by the laboratory scale button arc-melting process. Oxygen introduction raises concerns for the mechanical performance of these alloys if employed as structural materials alone or in engineering applications, such as serving as filler materials to enable joining of similar or dissimilar alloy pairs that are conventionally considered difficult to join. In this work, oxide inclusions in an as-cast off-equiatomic MnFeCoNiCu MPEA and Ni-base alloy braze joints made with this MPEA were evaluated by synchrotron x-ray diffraction mapping and electron microscopy. MnO was found to be prevalent throughout the cast MPEA and was chemically reduced during brazing by trace Al from the base material, Ni-base Alloy 600. Incomplete reaction of the MnO with Al, and some alternative reaction with Cr, left a mixture of MnO, Al_2O_3, and Cr_2O_3 in the as-brazed joint, with the oxides concentrated near the braze centerline due to directional solidification. In the braze joints, the non-oxide constituent phases detected were an FCC matrix and particles of $Cr_{23}C_6$, Cr_7C_3, and TiN which are all native to Alloy 600. The evolution of oxides within the brazed joints at elevated service temperatures of 600–800 °C was also evaluated. While MnO and Al_2O_3 were stable during high-temperature service, Cr_2O_3 particles grew to several hundred microns, with dissolved oxygen in the MPEA providing a significant source for oxide growth. Comparing tensile performance of the as-brazed condition with post-service conditions showed that the evolution of oxide particles contributed to an increase in strength and decrease in ductility of the brazed joints. Evaluating particle morphologies among fracture surfaces of individual specimens demonstrated that large Cr_2O_3 particles and continuous cluster networks of Al_2O_3 were the features most detrimental to total elongation. Hence, unmitigated evolution of oxygen-containing species during brazing and service conditions is detrimental to the ductility of the brazed joints, which highlights the importance of oxygen control in initial manufacturing of MPEAs for engineering applications.

1. Introduction

Multi-principal element alloys (MPEAs), which encompass high-entropy alloys (HEAs), have been gaining traction in the metallurgical community since 2004, when their potential beneficial effects were first published [1,2]. Today, MPEA research continues to accelerate and diversify, and manufacturing methods to produce new compositions for study are expanding accordingly [3]. Powder metallurgy (PM) mechanical alloying techniques have emerged as a solid-state alternative for producing certain MPEAs [3–6], but the predominant manufacturing strategy remains casting from the liquid state. The most common MPEA casting method reported in literature is laboratory-scale button arc-melting, particularly in studies which examine a multitude of distinct novel compositions, requiring an inexpensive and rapid means of synthesis [7–11]. In 2015, Jablonski et al. commented on several shortcomings of button arc-melting, including its tendency to result in solidification defects and macro-segregation, which cause variability in properties and are industrially unacceptable [12]. Vacuum induction melting (VIM) is a more relevant, industrial casting method preferred for solidification-sensitive alloys and critical applications that require strict compositional control. VIM offers more uniform solidification conditions [12] and better oxygen and trace element control, reducing the presence of microstructural defects and tramp elements when compared to “in air” casting processes [3]. Some recent MPEA studies have

* Corresponding author.
E-mail address: zyu@mines.edu (Z. Yu).

https://doi.org/10.1016/j.jmapro.2023.01.017
Received 12 September 2022; Received in revised form 6 December 2022; Accepted 5 January 2023
Available online 13 January 2023

employed VIM for casting [13,14], while others have incorporated induction melting in an inert gas environment [15].

Given the wide variability in manufacturing techniques and in the quality of fabrication equipment among various laboratory-scale research facilities, there is relatively little acknowledgment in the literature of the effects of contamination by atmospheric elements in MPEAs. There are two reasons for this lack of discussion: (1) MPEAs contain many elements of interest, such that contaminant interstitials are often ignored in compositional analyses [12], and (2) the majority of phase-stability research on MPEAs has been heavily focused on favoring solid solution phases over intermetallic compounds [16], such that any minor carbide, nitride, or oxide phases are frequently disregarded. The role of these contaminant phases is gaining attention, however. Some of the recent studies on MPEA production by PM techniques trace the origins of oxygen contamination throughout their MPEA manufacturing process and comment on the role of oxide phases in performance [4–6]. A handful of studies on cast MPEAs acknowledge the presence of contaminant oxides in their microstructure, but usually do not correlate their presence directly with the manufacturing conditions [7,12]. Choi et al. conducted a direct investigation of the effect of contaminant inclusions upon mechanical performance of the CrMnFeCoNi MPEA, achieving variable contamination levels and inclusion morphologies by altering the casting environment [17]. These authors demonstrated that fine oxide inclusions were more adverse to ductility, while coarse inclusions were more detrimental to ultimate tensile strength [17]. Thus, gaining better understanding of the effects of atmospheric element contamination and nature of the resultant inclusions is important for cast MPEAs for practical engineering applications.

Furthermore, recent studies on MPEA development as filler materials for joining applications indicated oxygen introduction into MPEAs during manufacturing is likely to adversely impact the mechanical performance of joined components as well. MPEA fillers developed for Ni-base alloy braze repair have included near-equiatomic MPEAs with added melting-point depressants [18–20] and off-equiatomic MPEAs designed to melt intrinsically at an appropriate temperature range for this application [21–25]. An off-equiatomic MPEA filler developed by the authors' research team for Ni-base alloy brazing, $Mn_{35}Fe_5Co_{20}Ni_{20}Cu_{20}$, has demonstrated success in avoiding brittle eutectic microconstituents and intermetallic phases, while providing comparable strength and far improved ductility over conventional fillers [25]. In brazing applications, cast MPEAs are designed to re-melt during filler delivery, experiencing non-negligible interactions with the base material in the process, and then be exposed to the high-temperature operating environment of the Ni-base alloy following brazing. Therefore, there are several opportunities for contaminant elements introduced during MPEA filler production to evolve within the system at elevated temperatures, possibly precipitating undesired phases that may adversely affect properties. The authors' previous work has suggested that variabilities in the quantity and morphology of contaminant oxides are responsible for variations in the ductility of MPEA-brazed Ni-Alloy 600 structures in tension [25], similar to findings discussed for bulk MPEAs [17]. This work aims to perform a comprehensive assessment of the contaminant particles present in the as-cast MPEA filler, and their evolution within the braze joints during brazing and subsequent service conditions. Synchrotron x-ray diffraction (XRD) and energy-dispersive spectroscopy (EDS) methods were used to examine the evolution of particles including carbides, nitrides, and oxides. The effects of contaminant phases on the mechanical performance of the MPEA-brazed structures were investigated.

2. Experimental procedures

2.1. MPEA filler production and oxygen evaluation

Ingots of MPEA filler of approximate composition $Mn_{35}Fe_5Co_{20}Ni_{20}Cu_{20}$ were arc melted directly from pieces of its pure constituent elements on a water-cooled copper hearth, using a gas-tungsten arc welding electrode encased in a stainless-steel environmental chamber assembled in-house [22,23]. Ingots were flipped and re-melted three times to ensure bulk compositional homogeneity. The chamber was evacuated with a mechanical pump and backfilled with ultra-high purity argon gas three times prior to each melt. However, the highest vacuum level achievable with this production setup was 0.9 Torr, measured by a type-531 thermocouple pressure gauge, causing appreciable oxygen to remain in the chamber atmosphere. Prior to each melt, a piece of titanium metal was melted inside the chamber and held molten for 20 s to attempt to bind remaining atmospheric oxygen. After casting, ingots were milled to uniform thickness, removing all visible surface oxide. Subsequently, the oxygen and nitrogen content of the as-fabricated MPEA filler were estimated using a Leco TCH600 inert gas fusion elemental analyzer, calibrated using steel calibration samples with a known oxygen content of 200 ppm and nitrogen content of 535 ppm.

2.2. Brazing

Samples of Alloy 600 were furnace-brazed using MPEA foil cold rolled to a thickness of 300 μm. Brazing was conducted at a vacuum level of 10^{-5} Torr or better as measured by an ion gauge, using a holding temperature of 1200 °C and a hold duration of 90 min followed by furnace cooling, as described in [23,25]. Two sample geometries were produced: a lap-joint of rectangular members with 1/4-in thickness [23], and a butt-joint of cylindrical rods with 3/8-in diameter [25]. The butt-joint configuration employed stainless-steel fixturing and Continental Braze Supply Pro-Stop 700V stop-off to keep the members axially aligned [25]. In both cases, the joint clearance was not fixed, and the plane of the joint gap was horizontal, with the uppermost Alloy 600 member allowed to weigh freely upon the molten MPEA filler during brazing [24].

2.3. Machining and heat treatment

Coupons 1 mm in thickness encompassing the entire braze cross-section were cut from the brazed lap-joints for characterization by synchrotron x-ray diffraction (XRD) and energy-dispersive spectroscopy (EDS). The cylindrical butt-joints were machined using a lathe into ASTM E8M round tensile samples with a gauge-section diameter of 6 mm and a 1 μm surface finish. After machining, some coupons and tensile samples were left in the as-brazed condition, while others were heat-treated in a Carbolite CWF-1200 open-air furnace at either 600 °C or 800 °C for 100 h, followed by water quenching. The open-air environment was selected to simulate industrially relevant service conditions. Selected coupons were also heat treated in an evacuated quartz tube for comparison. The heat treatment temperatures were selected to simulate a range of possible operating conditions for Alloy 600 and other Ni-base superalloys to which the MPEA filler could be potentially applied [26,27].

2.4. Characterizations

Both as-brazed and heat-treated tensile bars were mechanically tested to failure at room temperature on an MTS Landmark hydraulic load frame at a strain rate of 10^{-3} s^{-1}. Following testing, sample fractography was performed using an FEI Helios Nanolab 600i scanning electron microscope (SEM), with low-magnification EDS mapping performed to identify the composition of particles on the fracture surfaces. After standard metallographic preparation with a final polishing step of 0.05 μm colloidal silica, both as-brazed and heat-treated 1 mm thick coupons cut from the lap joints were analyzed by optical microscopy and EDS, performed using a Tescan S8252G SEM.

Synchrotron XRD patterns were collected from the as-brazed and heat-treated coupons at beamline 1-ID-E of the Advanced Photon Source. A monochromatic beam with energy of 61.332 keV was directed

in transmission through the 1-mm thick samples, with incident beam dimensions of 100 μm horizontally by 50 μm vertically. A Pilatus3X CdTe 2M hybrid photon counting detector with a sample-to-detector distance of 740 mm was used to collect patterns. The coupons were positioned with the plane of the braze horizontal and translated horizontally and vertically in increments equal to the dimensions of the incident beam. This translation created a continuous spatial map of XRD patterns that extended 500 μm in either direction from the braze centerline, and laterally over the full width of the braze coupon.

Individual synchrotron XRD patterns were also collected from samples of the MPEA foil itself. To increase the diffracting grain population and achieve a near-powder pattern for easier observation of minor constituent phases, MPEA for synchrotron characterization was rolled at 400 °C to 50 % reduction in thickness, and subsequently recrystallized at 850 °C for 2 h in an evacuated quartz tube. This processing decreased the grain size from >100 μm in the as-cast state to the range of 10–40 μm in the recrystallized state. Light surface oxidation occurred during the recrystallization treatment and was removed with SiC grinding paper prior to synchrotron characterization.

3. Results

3.1. Microstructure evolution during service

Fig. 1(a) illustrates a synchrotron XRD pattern taken from the MPEA recrystallized as described above, plotted against the wavelength-independent reciprocal lattice vector q = 2π/d, where *d* is the interplanar atomic spacing. It should be noted that in the authors' previous diffraction studies within the as-cast MPEA [28], a strong solidification texture was observed along with obvious shoulder peaks corresponding to interdendritic segregation. Such features were eliminated by the recrystallization treatment, allowing for easier observation of minor phase peaks than the previous diffraction study on as-cast MPEA. The diffraction pattern is consistent with a major FCC phase containing MnO particles. Fig. 1(b) provides an SEM image and corresponding EDS element maps of one such MnO particle. Fig. 1(b) was generated from MPEA filler in the as-cast condition, proving that MnO particles are introduced in the casting process, before the recrystallization treatment employed for easier observation by XRD. Furthermore, the estimated total oxygen content of the as-cast MPEA by inert gas fusion elemental analysis was 1648 ± 160 ppm. While this quantity is only an estimate because it is far beyond the calibration curve provided by the steel calibrant, the oxygen content is certainly several times greater than 40–50 ppm, the level reported in MPEAs fabricated by VIM [12,13]. The estimated nitrogen content of the MPEA in this work was 2040 ± 241 ppm, which is also far greater than what could be achieved under optimal VIM conditions. Previous mechanical testing on the as-cast MPEA demonstrated a highly ductile deformation response despite the level of oxygen introduced during manufacturing [23], but the presence of MnO particles indicates that further improvements to performance are achievable with better environmental control.

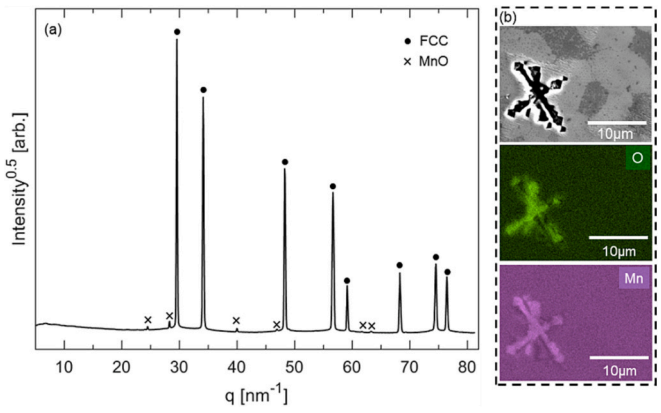

Fig. 1. (a) Synchrotron XRD pattern taken from the MPEA following rolling at 400 °C to 50 % reduction in thickness and recrystallization at 850 °C for 2 h. (b) SEM image and EDS Mn and O maps of an MnO particle found in the as-cast MPEA.

Figs. 2, 3, and 4 compile EDS and synchrotron XRD data from MPEA-brazed Alloy 600 coupons in the as-brazed condition, the 600 °C-100 h heat-treated condition, and the 800 °C-100 h heat-treated condition, respectively. Figs. 2(a), 3(a), and 4(a) provide optical macrographs of the entire braze cross-section, with the grid of red rectangles indicating the size and position of individual incident beams used to construct the spatial maps of XRD patterns. Note that only a single row and column of beam positions is shown so that the macrograph is clearly visible, but spatial mapping was conducted in a grid over the entire rectangular area indicated by the dashed outline. For each sample, patterns were averaged laterally across the *y* dimension indicated in the figures. This analysis approach was undertaken to investigate how the constituent phases indicated by the XRD patterns varied over the spatial coordinate *x*, as indicated in the figures, where *x* is defined as the absolute value of the distance from the braze centerline.

In all cases, deviations from powder texture, along with compositional complexity, presented challenges in identifying constituent phases via automated software packages based upon the powder diffraction file. Instead, XRD peak positions were identified by fitting a Pearson VII peak function [29] to the data. Peak positions were then compared to simulated patterns of likely constituent phases identified using composition information from EDS, and using published Alloy 600 technical data [26]. Simulated patterns were produced using GSAS-II [30]. Consistency of peaks among similar locations on the spatial map, the potential for peak shifting due to atomic substitution in a concentrated alloy environment, and the simulated powder intensities among candidate phases were all considered when identifying the phase that produced each peak.

Fig. 2(b-1) and (b-2) indicate that in the as-brazed condition, dispersed particles rich in Ti and N exist throughout the base material and the filler region, while Fig. 2(b-6) and (b-7) show that dispersed particles rich in Al and O populate a region near the centerline. The segregation morphology most commonly presented among the major constituent elements is displayed, showing continuous (Mn, Cu) grain-boundary segregation along the immediate centerline in the filler region in Fig. 2(b-8, b-10), thought to represent the last material to solidify [23,24]. Fig. 2(c) and (d) show selected EDS data demonstrating other phenomena found in as-brazed samples. Fig. 2(c) shows a region with a much denser distribution of (Al, O) rich particles, while Fig. 2(d) shows a region with no (Mn, Cu) segregation. Unsegregated brazes such as in Fig. 2(d) are found intermittently among samples and usually occur in regions where the final thickness of the filler region is limited to under 200 μm, suggesting that there is a dependency of segregation on the local joint clearance, with regions displaying a narrower gap being less prone to segregation. Joint clearance is uncontrolled in the brazing setup and may vary due to imperfect mating between faying surfaces. Greater local joint clearances will increase the amount of interspace that must be back-filled following solidification of the initial grains growing epitaxially from the substrate surface, causing more opportunity for Mn- and Cu-rich liquid to coagulate in this space at the end of the solidification sequence. Additionally, prior work in which the joint clearance was fixed at a wide-gap value of 1 mm displayed even more pronounced segregation in the final regions of the material to solidify than is observed in this study [24].

In all conditions, XRD patterns display an FCC solid solution phase as the primary microstructural constituent for all locations across the joint (*x* axis in Fig. 2(a)). As annotated in Fig. 2(b-9), the measured lattice parameters are 3.631 Å for the (Mn, Cu) segregation region within the filler, 3.602 Å for the (Co, Fe) rich filler regions, and 3.561 Å for the Alloy 600 base material. Patterns such as that in Fig. 2(e), taken from *x*

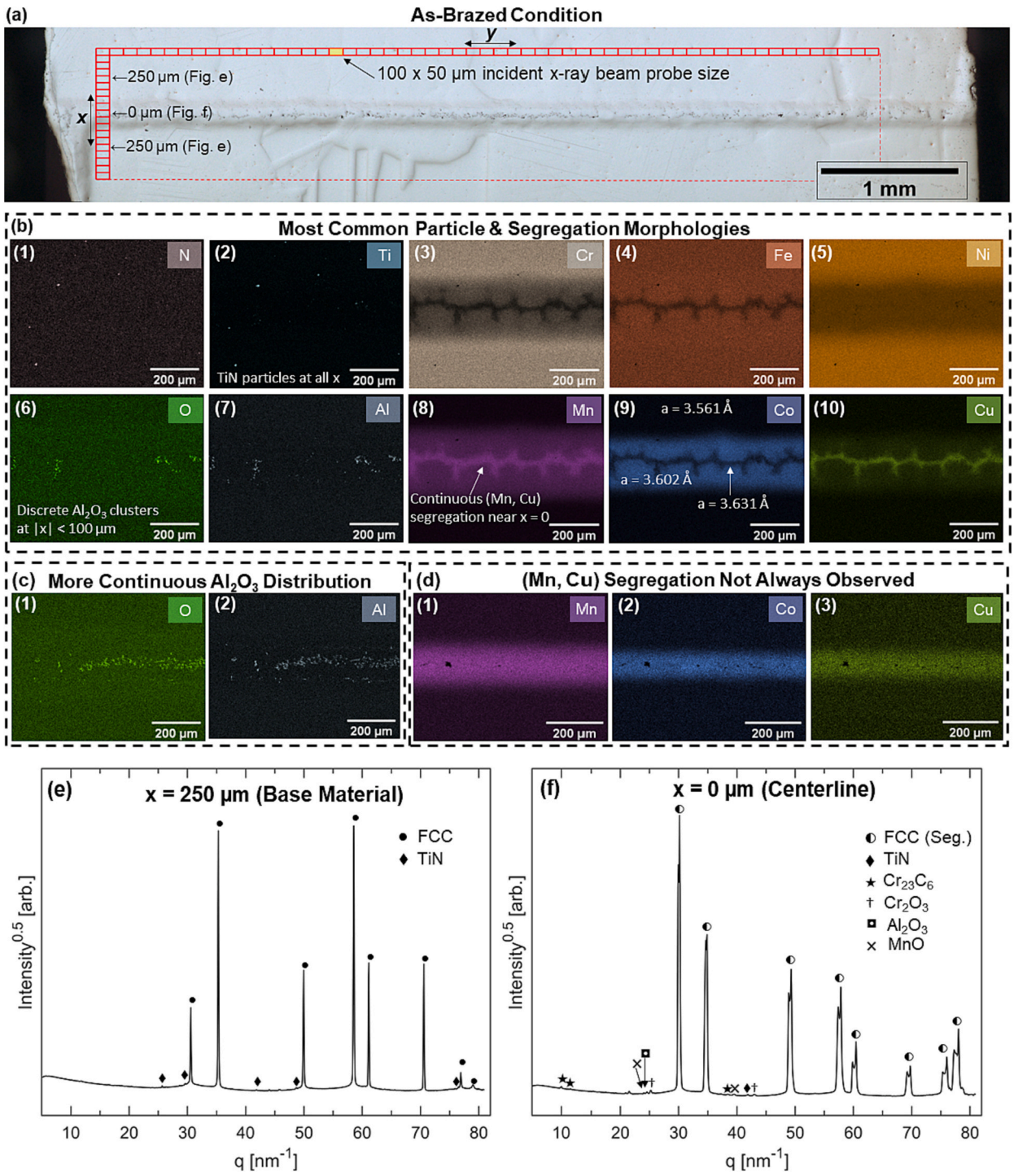

Fig. 2. The as-brazed condition: (a) Optical macrograph with incident beam positions indicated by the red rectangles. (b-d) Selected EDS element maps displaying (b) the most common particles and segregation morphologies; (c) a region with a denser Al_2O_3 dispersion, and (d) a region with no (Mn, Cu) segregation. (e-f) Synchrotron XRD patterns collected at (e) x = 250 μm and (f) x = 0 μm. (For interpretation of the references to colour in this figure legend, the reader is referred to the web version of this article.)

= 250 μm, confirm the presence of TiN. Though Alloy 600 nominally contains no Ti, TiN is reported as a minor phase in its microstructure [26]. The peak positions for TiN are extremely consistent at all values of *x*, indicating this phase is inert and displays little if any substitutional uptake of other elements from its environment. Fig. 2(f) demonstrates the additional presence of three oxide phases – Cr_2O_3, Al_2O_3, and MnO – at the immediate centerline, with the Al_2O_3 phase being the most visible in the EDS data. $Cr_{23}C_6$, a reportedly stable carbide in Alloy 600 below 760 °C, is also present [26]. The centerline XRD pattern displays peak splitting resulting from simultaneous diffraction of the (Mn, Cu) and (Fe, Co) rich filler regions, segregation, which have a 0.8 % disparity in lattice parameter, similar to the phenomenon reported in [28].

As seen in Fig. 3(a-b), little change relative to the as-brazed condition is observed after 100 h at 600 °C in either the optical macrograph or the EDS data. Fig. 3(c) demonstrates that very small $Cr_{23}C_6$ peaks were observed in the base material following this heat treatment, and Fig. 3

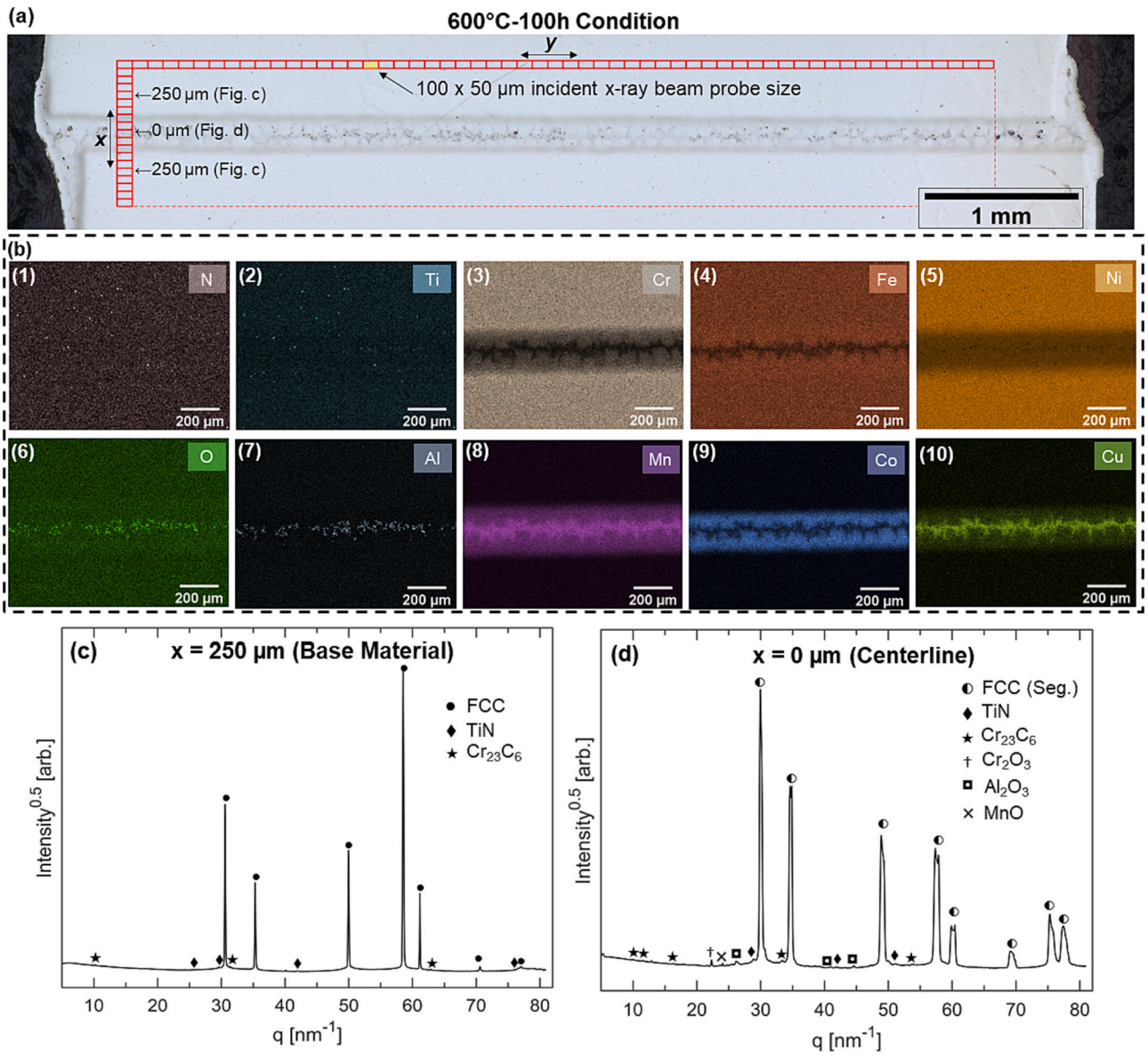

Fig. 3. The 600 °C-100 h condition: (a) Optical macrograph with incident beam positions indicated by the red rectangles. (b) EDS maps showing element distribution in this condition. (c-d) Synchrotron XRD patterns collected at (e) x = 250 µm and (f) x = 0 µm. (For interpretation of the references to colour in this figure legend, the reader is referred to the web version of this article.)

(d) illustrates the centerline presence of the same three oxide phases as in the as-brazed condition.

Fig. 4 indicates that more significant changes occur during the 100-h heat treatment at 800 °C. Cr_2O_3 and Al_2O_3 precipitation during heat treatment is evident in both EDS and XRD data. Particles rich in both chromium and oxygen are observed in Fig. 4(b-3, b-6), while Fig. 4(c) shows that some large Cr_2O_3 peaks are observed in XRD patterns extending into the base material. Fig. 4(d) shows that Cr_2O_3, Al_2O_3, and MnO are all still present at the centerline. The EDS data in Fig. 4(b-8) also shows a depletion of Mn along grain boundaries that were previously enriched in Mn and Cu, and remain enriched in Cu after heat treatment, as shown in Fig. 4(b-10). Mn is the most volatile constituent element of the filler, with a vapor pressure of 1.6×10^{-4} Torr at 800 °C, 1000 times greater than that of Cu, the next most volatile constituent [31]. This volatility makes Mn prone to vaporization in certain regions where Mn is segregated along grain boundaries that are connected to the specimen surface (see Fig. 4a). This vaporization is limited in extent to regions that possess a continuous (Mn, Cu) segregation in the as-brazed state, as is evident by the absence of Mn depletion on the left-hand side of Fig. 4(b-8), where the Cu segregation in Fig. 4(b-10) is also absent. Cu-segregation is left unchanged by heat treatment.

Fig. 5 compares the spatially dependent intensities of the maximum XRD peak for each non-major phase in the as-brazed condition and the two heat-treated conditions. The approximate extent of the MPEA filler in *x* is denoted. As indicated, the minor phases that formed during brazing and service were limited to nitrides, carbides, and oxides, with no intermetallic phases detected. While a Rietveld refinement to quantitatively calculate phase fractions was not feasible because of the same challenges that prevented automated phase identification, Fig. 5 offers a semi-quantitative comparison of the phases observed in all three conditions. The size, volume fraction, and proximity to an orientation meeting the Bragg condition for discrete particles all play a role in determining intensity.

Fig. 5(a-c) illustrate the incorporation of TiN, $Cr_{23}C_6$, and Cr_7C_3 – three phases native to Alloy 600 [26] – into the MPEA filler region. TiN and $Cr_{23}C_6$ are present at all *x* across all three conditions, while Cr_7C_3

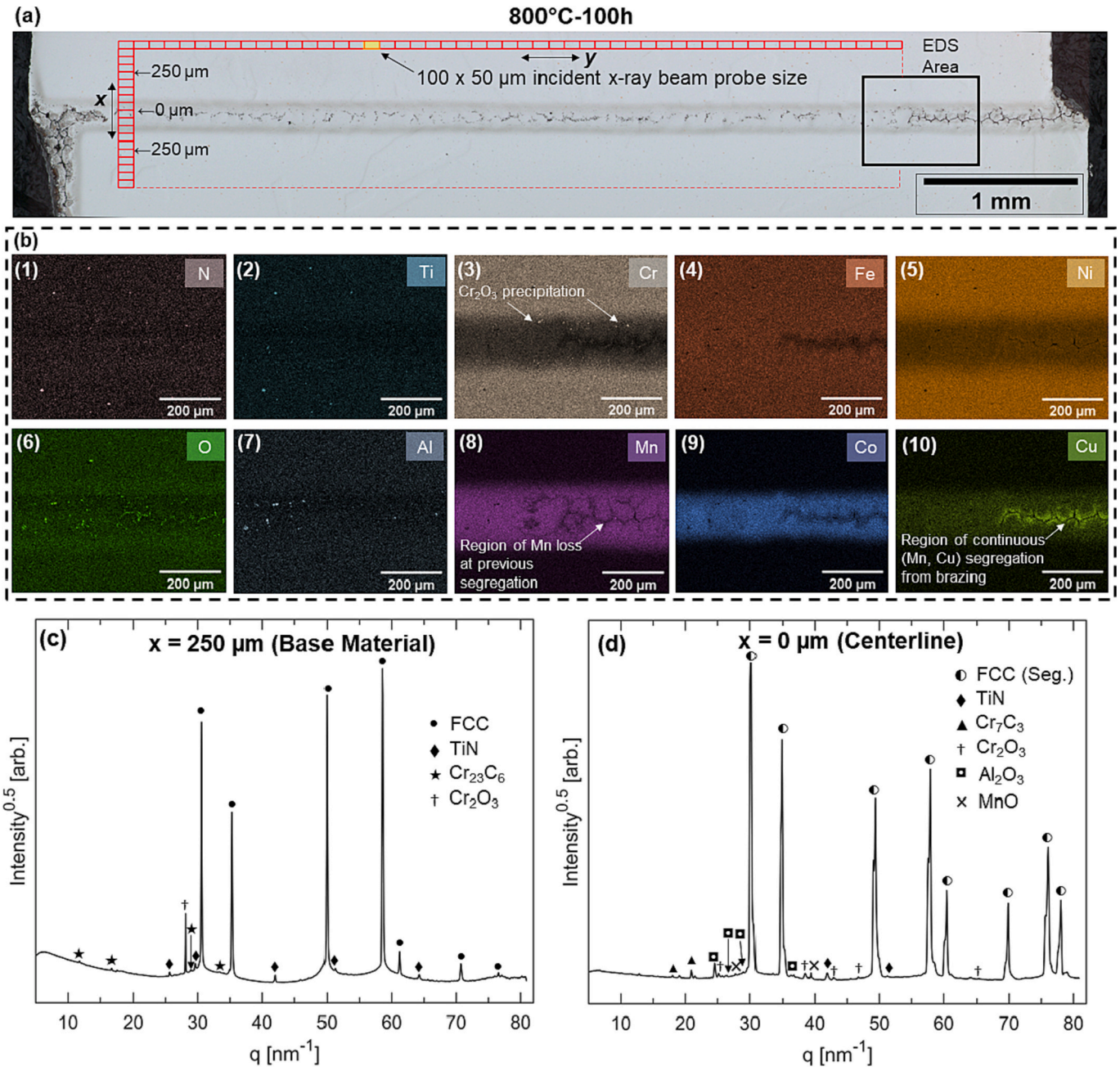

Fig. 4. The 800 °C-100 h condition: (a) Optical macrograph with incident beam positions indicated by the red rectangles and EDS map area shown by the black rectangle. (b) EDS element maps displaying the most common particle and segregation morphologies. (c-d) Synchrotron XRD patterns collected at (e) x = 250 µm and (f) x = 0 µm. (For interpretation of the references to colour in this figure legend, the reader is referred to the web version of this article.)

appears more intermittently. Heat treatment at 600 °C almost completely suppresses the Cr_7C_3 phase, while it is more prevalent in the as-brazed condition and after heat treatment at 800 °C. This behavior is consistent with the reported favorability of Cr_7C_3 above 760 °C [26]. For TiN and $Cr_{23}C_6$, the highest intensity generally occurs in or near the filler region, which may indicate concentration and/or growth of these particles within the filler due to high nitrogen and potentially carbon content in the cast MPEA.

The behavior of the oxide phases in Fig. 5(d-f) is the most important takeaway from Fig. 5. Al_2O_3 and MnO are only found at $x \leq 200$ µm, approximately coincident with the filler region. The intensity of these two oxide phases is comparable between the as-brazed condition and the 600 °C-100 h condition, but a notable increase in the intensity of both phases is observed after heat treatment at 800 °C, which may indicate some growth of Al_2O_3 and MnO particles at this temperature. Cr_2O_3 is present further from the centerline than either Al_2O_3 or MnO in all conditions, owing to the abundance of Cr in the base Alloy 600. In the as-brazed condition, the intensity of Cr_2O_3 is small and usually limited to near the centerline. After heat treatment at 600 °C, more intense Cr_2O_3 peaks are observed in a few patterns extending up to $x = 450$ µm, while after heat treatment at 800 °C, these large Cr_2O_3 peaks are more consistent and widespread. The data are consistent with the precipitation of some Cr_2O_3 particles during 600 °C heat treatment and more numerous or larger Cr_2O_3 particles during 800 °C heat treatment.

To supplement the diffraction intensity data in Fig. 5, Fig. 6 compares cross-sectional SEM micrographs of the as-brazed microstructure and the microstructure following heat-treatment at 800 °C for 100 h. The MPEA filler and base material regions were delineated via EDS

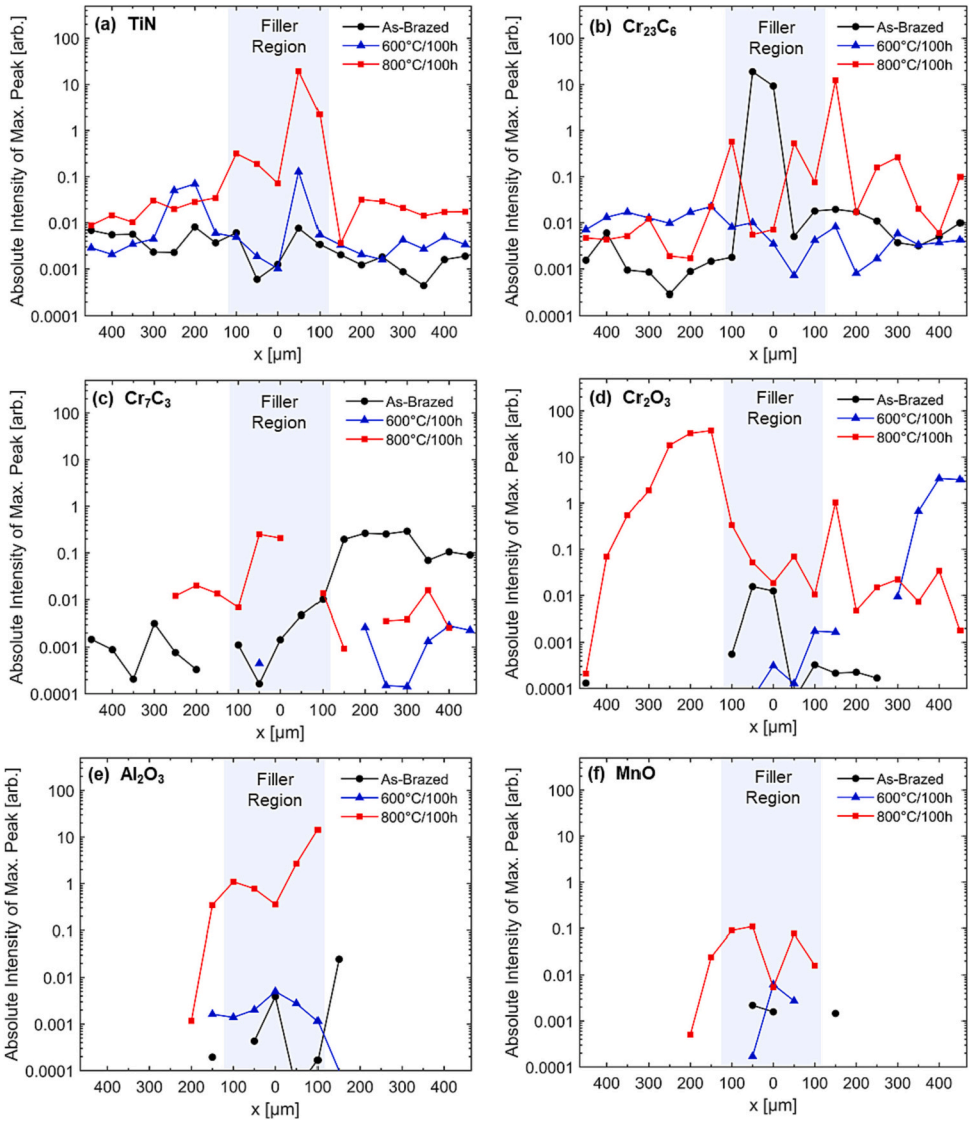

Fig. 5. Intensities of the maximum peak for each minor phase identified as a function of distance from the braze centerline for the as-brazed condition and two heat-treated conditions. (a) TiN. (b) $Cr_{23}C_6$. (c) Cr_7C_3. (d) Cr_2O_3. (e) Al_2O_3. (f) MnO.

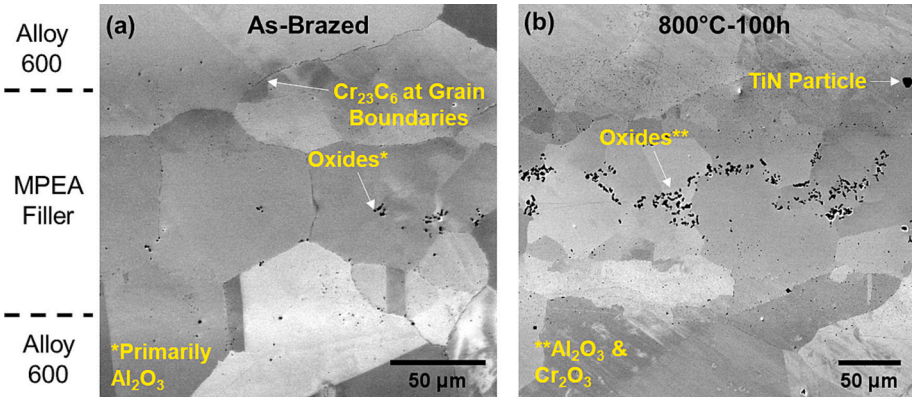

Fig. 6. SEM micrographs of the brazes in (a) the as-brazed condition and (b) the 800 °C-100 h condition, highlighting examples of the distribution of the phases detected by synchrotron XRD.

elemental mapping and are indicated at the left side of the figure. This EDS mapping was also employed to identify instances of the phases reported in Fig. 5. Fig. 6(a) shows examples of grain-boundary precipitates identified as chromium carbides, consistent with the occurrence of the $Cr_{23}C_6$ phase throughout the braze structure in Fig. 5(b). An example of a TiN particle is indicated in Fig. 6(b), consistent with the diffraction

intensity for this phase throughout the microstructure in Fig. 5(a). Oxide particles are identified in both Fig. 6(a) and (b). While the discussion of Fig. 2 notes that there is regional variation in the as-brazed oxide particle distribution, this density of the distribution generally increases after 800 °C-100 h heat treatment, as exemplified in Fig. 6. Much of this increase in the number of observable oxides is attributable to the growth of discrete Cr_2O_3 particles, as indicated by the increased diffraction intensity in Fig. 5(d) and discussed further throughout Section 3.2.

3.2. Effect of oxides on mechanical performance

Fig. 7 summarizes the results of mechanical testing on the MPEA-brazed Alloy 600 tensile bars machined from butt joints for the as-brazed, 600 °C-100 h, and 800 °C-100 h conditions. All samples failed at the braze interface. A slight increase in both yield strength and ultimate tensile strength (UTS) of the brazes was observed following either heat treatment, alongside an accompanying decrease in ductility. Overall, the specimens heat treated at 600 °C demonstrated slightly higher strength and lower ductility than those heat treated at 800 °C. The mean yield strength increased from 217 MPa in the as-brazed condition to 269 MPa after heat treatment at 600 °C and 238 MPa after heat treatment at 800 °C. The UTS followed a similar trend, increasing from 332 in the as-brazed condition to 360 MPa after 600 °C-100 h and 358 MPa after 800 °C-100 h. The mean total elongation decreased from the as-brazed value of 12.5 % to 2.3 % in the 600 °C-100 h condition and 3.5 % in the 800 °C-100 h condition. As indicated by the inset of Fig. 7 (a), significant variability in the total elongation was observed among specimens in each heat-treated condition, as well as in the as-brazed condition shown in the main part of the figure.

To understand the variability in performance among the heat-treated specimens, fractography was performed on the best-performing and worst-performing specimen in each condition. Fig. 8 shows low-magnification SEM micrographs and corresponding EDS element maps for Cr, Al, and O for each of these specimens. EDS is not a quantitative technique when performed on a tortuous fracture surface, and the elemental distribution maps in Fig. 8 do not account for local variations in topography, which may affect the overall counts at the EDS detector. However, EDS can nonetheless assist in identifying particles on the fracture surfaces. These EDS maps supplement the assessments of the oxide phases from cross-sectional EDS and synchrotron XRD discussed in Section 3.1 and offer insights into the mechanical performance of the specimens.

Fig. 8(a) shows that few Cr_2O_3 particles and discrete clusters of Al_2O_3 exist on the fracture surface of the best-performing specimen in the 600 °C-100 h condition. For the worst-performing specimen in this condition (Fig. 8(b)), numerous Cr_2O_3 particles up to 200 μm in length are observed, alongside a continuous network of Al_2O_3. The inconsistent precipitation of Cr_2O_3 at 600 °C agrees with the XRD peak intensity data in Fig. 5(d). Fig. 8(c-d) show that large Cr_2O_3 particles are found on fracture surfaces of both the best-performing and worst-performing specimens heat treated at 800 °C, with the largest particles exceeding 500 μm in length, in agreement with the widespread high Cr_2O_3 intensity in Fig. 5(d). The coarser Cr_2O_3 morphology in the 800 °C condition are consistent with the slightly lower strength and higher ductility observed relative to the 600 °C condition in Fig. 7, according to the findings of Choi et al. [17]. The Al_2O_3 distribution was found to be similar between the two fracture surfaces in Fig. 8(c) and (d), consisting of discrete clusters of particles. However, the worst-performing specimen heat-treated at 800 °C also displayed a region of incomplete fill, a brazing defect identifiable by the preserved dendrite tips observable to the right of the yellow dashed line in the SEM micrograph in Fig. 8(d). While the background oxygen level in the region of incomplete fill in Fig. 8(d) appears only marginally greater than that on the fracture surface, the working distance to the SEM pole piece was significantly longer in the region of incomplete fill since this area did not lengthen during the tensile test. In the EDS map, which does not account for topographic variations, the background oxygen level may appear artificially low in the defect area, since this area was exposed to air at high temperature during heat treatment. Despite the larger working distance in the defect area, the apparent background Cr content is nonetheless elevated. This observation further indicates incomplete fill during brazing, as Fig. 2(b) indicates that the final liquid to solidify at the braze centerline is lean in Cr in segregated regions of a braze, so the elevated Cr content in the defect area indicates that this final liquid did not flow into this region. The defect area, caused by imperfect surface mating and serving as a pre-existing crack during tensile testing, was determined by macroscopic fractography to encompass 6.7 % of the fracture surface by area. This finding explains the lower ductility demonstrated by this specimen.

Fig. 9 shows higher magnification SEM images of the regions indicated in Fig. 8. Fig. 9(a-b) demonstrate brittle cracking through a fractured Al_2O_3 particle and Cr_2O_3 particle, respectively. In contrast, the surrounding matrix phase displays ductile microvoid coalescence (labeled MVC), indicating the oxides play a role in limiting the ductility of the heat-treated brazes. The region of incomplete fill in Fig. 8(d) allows for the examination of particles in their unfractured state. An unfractured Cr_2O_3 particle is shown in Fig. 9(c). This figure indicates the particles are rod-like in morphology with hexagonal crystallographic facets. The hexagonal facets further assist to positively identify the large Cr-rich particles visible in EDS as Cr_2O_3, which has a trigonal crystal

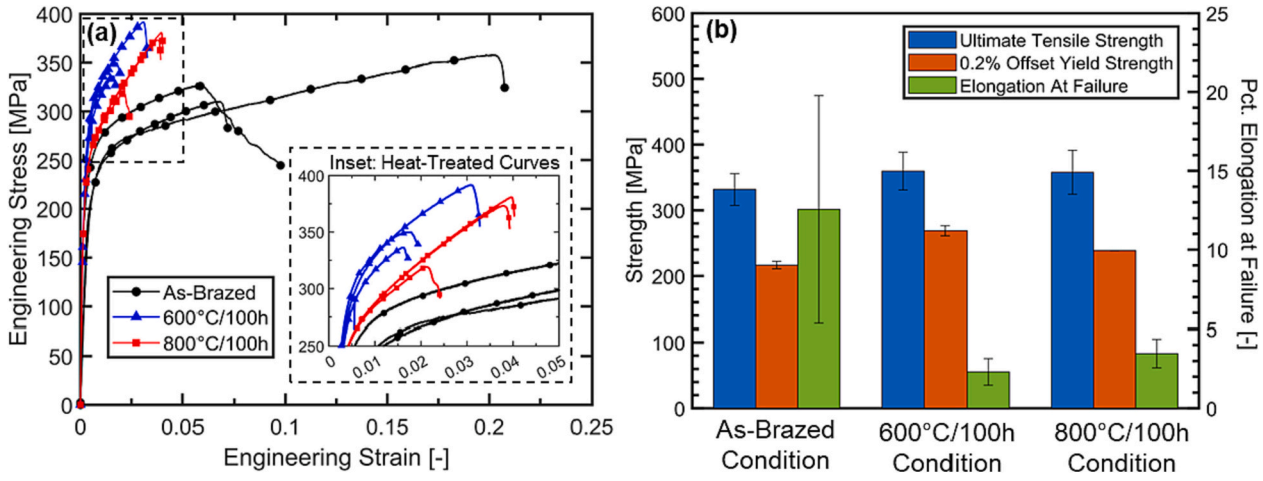

Fig. 7. Comparison of tensile data for the as-brazed, 600 °C-100 h, and 800 °C-100 h conditions. (a) Individual engineering stress-strain curves from mechanical testing; (b) summary of ultimate tensile strength, yield strength, and total elongation for the three conditions.

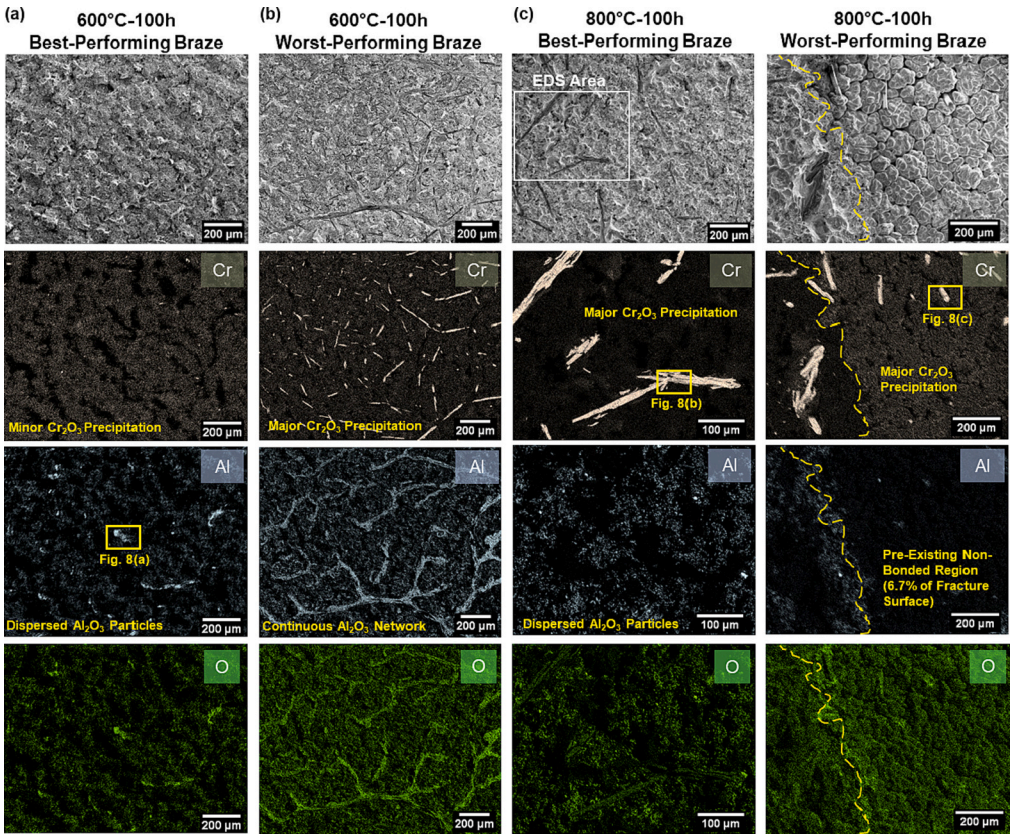

Fig. 8. Low magnification SEM fractography images and corresponding EDS maps for Cr, Al, and O for tensile specimens heat treated at (a-b) 600 °C-100 h and (c-d) 800 °C-100 h. (a, c) Best-performing tensile specimens; (b, d) worst-performing tensile specimens.

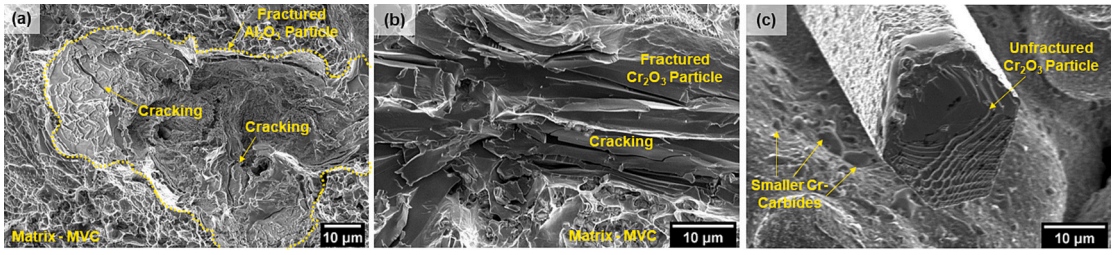

Fig. 9. Higher magnification SEM micrographs of fracture surface particles. (a) Fractured Al_2O_3 particle from the region indicated in Fig. 8(a). (b) Fractured Cr_2O_3 particle from the region indicated in Fig. 8(c). (b) Unfractured Cr_2O_3 particle from the region indicated in Fig. 8(d).

structure within the hexagonal crystal family and can produce hexagonal facets [32]. In contrast, $Cr_{23}C_6$ and Cr_7C_3 are cubic and orthorhombic, respectively [32], and thus neither carbide phase is capable of producing the observed hexagonal morphology. Smaller Cr-rich particles, identified by EDS and believed to be chromium carbides, also decorate the surface of the incomplete fill region and are visible in Fig. 9 (c).

4. Discussion

The maximum vacuum capability of 0.9 Torr in the MPEA production chamber, the presence of MnO in the as-fabricated MPEA, and the estimated oxygen content of 1648 ± 160 ppm all indicate insufficient control of atmospheric oxygen during MPEA production. Little additional oxygen introduction is likely during brazing, as the brazing chamber is held at much higher vacuum (10^{-5} Torr). During exposure to service conditions in the open air, environmental oxygen atoms may diffuse from the surface to the interior of the braze along grain boundaries or defect networks, and oxygen atoms dissolved in the FCC matrix may precipitate oxides to alleviate supersaturation as the system evolves toward equilibrium. Cr_2O_3 was observed to precipitate in specimens heat treated in an evacuated quartz tube in addition to those heat treated in the open air. This finding indicates that oxide precipitation during simulated service results primarily from the diffusion of excess dissolved oxygen rather than from environmental introduction. Furthermore, the size of the observed oxide particles on fracture surfaces was not generally a function of distance from the specimen surface. If oxygen diffusing from the furnace environment were the primary source for precipitation, larger oxide particles would generally populate more superficial regions.

Fig. 10 provides a schematic illustration of the behavior of oxygen in the MPEA-Alloy 600 system after it has been introduced through MPEA filler production. Before brazing (Fig. 10a), MnO is the preferred oxide in the as-fabricated MPEA because Mn has the greatest affinity for oxygen out of the MPEA constituents according to the Ellingham diagram [33]. Given the high estimated oxygen content and non-equilibrium solidification of the MPEA during production by casting, the matrix is also supersaturated in dissolved oxygen, indicated by the dark blue colour in Fig. 10(a).

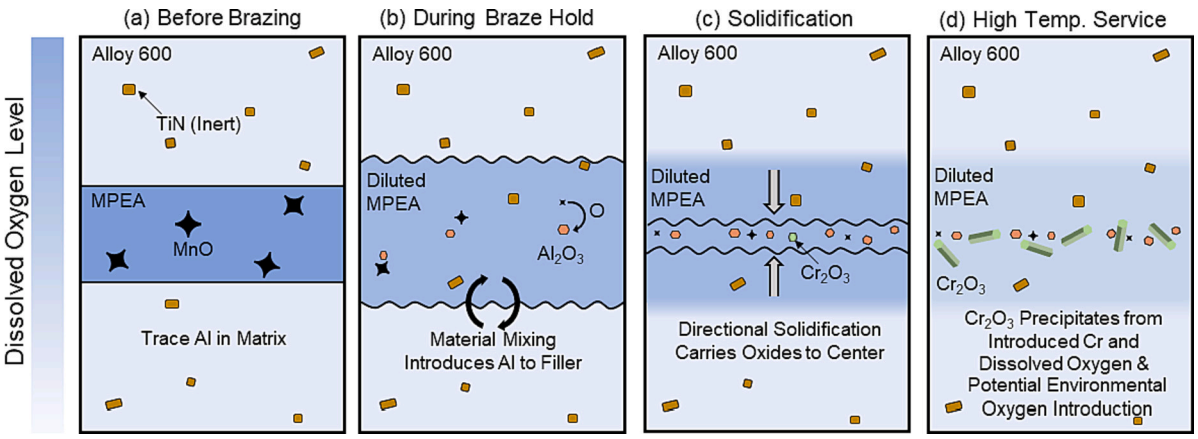

Fig. 10. Schematic illustration of the behavior of oxygen in the MPEA-Alloy 600 system during brazing and subsequent service. The following stages are illustrated: (a) before brazing, (b) during braze hold, (c) during solidification, and (d) during high temperature service.

During brazing (Fig. 10b), a degree of substrate dissolution will occur [25,34], diluting the total oxygen concentration in the molten filler and introducing Al from the Alloy 600 base material. Although Alloy 600 does not nominally contain Al, no maximum Al content is indicated in its compositional specification [26]. Furthermore, the material is produced in the same facilities as other Ni-base superalloys containing Ti and Al as γ'-formers, allowing some degree of cross-contamination to occur. Even trace Al contamination can result in Al_2O_3 formation, owing to the strong affinity of Al for oxygen, as indicated by the Ellingham diagram [33]. This phenomenon is well-documented in literature. Choi et al. found Al_2O_3 inclusions to occur in as-fabricated CoCrFeMnNi MPEAs as the result of trace Al impurities with an average concentration of 800 ppm among the nominally pure constituent elements [17]. A mixed Mn-Cr-Al oxide was observed in the same MPEA at Al concentrations as low as 130 ppm [14]. Thus, during the braze hold, trace Al from Alloy 600 chemically reduces MnO via the reaction

$$2Al + 3MnO \rightarrow 3Mn + Al_2O_3$$

causing pre-existing MnO particles to shrink at the expense of Al_2O_3 precipitation, as illustrated in Fig. 10(b).

When the braze hold is terminated, directional solidification often occurs (Fig. 10c) [23], causing the segregation observed in Fig. 2(b). Oxides which float in the liquid are carried to the braze centerline and coagulate there, explaining the Al_2O_3 distribution in the as-brazed condition observed in Fig. 2(b-c). Fig. 5(a) indicates the presence of MnO and Cr_2O_3 near the centerline as well; they occur because there is only a trace amount Al in the system, which is insufficient to bind all the contaminant oxygen. With the Ti in the system bound in inert TiN particles, the Ellingham diagram indicates the constituents with the next-greatest affinity for oxygen are Mn and Cr, whose affinities are similar [33]. MnO particles are likely those present in the original MPEA filler that did not undergo complete reaction with Al, while Cr_2O_3 results from new precipitation, which is possible because substrate dissolution has introduced significant Cr to the molten filler.

Following non-equilibrium solidification after brazing, the filler region remains significantly supersaturated in dissolved oxygen atoms, allowing the growth of existing oxides and the precipitation of new ones during high temperature service (Fig. 10d). Figs. 4, 5, and 8 all indicate that the preferred oxide to precipitate and grow is Cr_2O_3, as both chromium and dissolved oxygen are readily available in the filler region. Fig. 5(c) indicates that growth of existing Al_2O_3 is also possible during service, particularly at 800 °C. MnO present in the as-brazed condition is not observed to change appreciably during service conditions.

The effect of oxide particles on the mechanical performance of the MPEA brazes following service conditions has not been isolated in this study. Other microstructural changes, such as chromium carbide precipitation and Mn vaporization along grain boundaries, occur simultaneously during heat treatment. However, Figs. 7, 8, and 9 demonstrate that the oxides are an important factor in limiting ductility. In Fig. 7(a), the best-performing specimen heat-treated at 600 °C exhibited nearly twice the total elongation of the worst-performing specimen. A comparison of Fig. 8(a) and (b) shows a stark difference in the number and size of both Cr_2O_3 and Al_2O_3 on their fracture surfaces, likely resulting from an uneven distribution of oxygen in the original MPEA cast ingots. Fig. 9(a) and (b) demonstrate the brittle nature of each oxide particle, and the large size of precipitated Cr_2O_3 particles after both 600 °C and 800 °C heat treatments indicates significant influence on ductility of braze joints.

Overall, despite the oxide precipitation at both 600 °C and 800 °C conditions, the potential for incomplete fill brazing defects (Fig. 8d), and Mn vaporization damage at 800 °C (Fig. 4a), Fig. 7(a) shows that all specimens underwent yielding and appreciable plastic deformation prior to failure. This is not the case for Alloy 600 brazes produced using a conventional non-MPEA filler, which produces joints that contain chromium borides [25]. These findings illustrate that the MPEA's FCC matrix ensures ductile deformation and avoids fully brittle failure in the face of oxide inclusions, brazing defects, and defects acquired during service. Moreover, the constituent phase assessment did not detect any intermetallic phase precipitation during either 600 °C or 800 °C heat treatment, indicating the thermodynamic stability of the FCC solid solution matrix and the potential for enduring ductility in the braze filler if contamination from manufacturing is better controlled.

5. Conclusions

1. For the MPEA-brazed Alloy 600 system, the presence of MnO in as-fabricated MPEA, the poor vacuum capabilities of the MPEA arc-melting setup, and the high MPEA oxygen content estimated through inert gas fusion elemental analysis all point to the MPEA casting process as the primary point of oxygen introduction.
2. A comprehensive analysis by synchrotron XRD and EDS indicates that the MPEA-brazed Alloy 600 structure contains only the variably segregated FCC solid solution matrix phase and carbide, nitride, and oxide phases both before and after simulated service at 600 °C or 800 °C. No intermetallic phases are detected to form during brazing or simulated service for the heat treatments employed in this work. The carbide and nitride phases are native to Alloy 600, but the oxide phases result from atmospheric contamination of the filler.
3. During brazing, MnO reacts with trace Al from Alloy 600 to form Al_2O_3, which exists in the as-brazed microstructure alongside some Cr_2O_3 and unreacted MnO. During service at both 600 °C and 800 °C,

large Cr_2O_3 particles precipitate from available Cr and oxygen dissolved in the matrix.
4. Large Cr_2O_3 particles and Al_2O_3 cluster networks are identified as features detrimental to the ductility of brazes following simulated service. Improvements to performance can be expected with fewer contaminant particles, highlighting the importance of careful atmospheric oxygen control during MPEA production by casting.

Declaration of competing interest

The authors declare that they have no known competing financial interests or personal relationships that could have appeared to influence the work reported in this paper.

Acknowledgements

This research is supported by the National Science Foundation with Award No. 1847630. This research used resources of the Advanced Photon Source, a U.S Department of Energy (DOE) Office of Science User Facility operated for the DOE Office of Science by Argonne National Laboratory under Contract No. DE-AC02-06CH11357. Data was collected at Beamline 1-ID-E. Support from beamline staff was greatly appreciated. Use of the Tescan S8252G SEM was supported by the National Science Foundation Division of Materials Research Award No. 1828454.

References

[1] Cantor B, Chang I, Knight P, Vincent A. Microstructural development in equiatomic multicomponent alloys. Mater Sci Eng A 2004;375:213–8.
[2] Yeh JW, Chen SK, Lin SJ, Gan JY, Chin TS, Shun TT, Tsau CH, Chang SY. Nanostructured high-entropy alloys with multiple principal elements: novel alloy design concepts and outcomes. Adv Eng Mater 2004;6(5):299–303.
[3] Alshataif YA, Sivasankaran S, Al-Mufadi FA, Alaboodi AS, Ammar HR. Manufacturing methods, microstructural and mechanical properties evolutions of high-entropy alloys: a review. Met Mater Int 2020;26:1099–133.
[4] He J, Qiao Y, Wang R, Tang Y, Li S, Liu X, Ye Y, Zhu LA, Wang Z, Bai S. State and effect of oxygen on high entropy alloys prepared by powder metallurgy. J Alloys Compd 2021;891(161963).
[5] Fourmont A, Le Gallet S, Hoummada K, Descoins M, Desgranges C, Politano O, Baras F. Effects of mechanical activation on chemical homogeneity and contamination level in dual-phase AlCoCrFeNi high entropy alloy. Mater Chem Phys 2021;272:125000.
[6] Moravcik I, Kubicek A, Moravcikova-Gouvea L, Adam O, Kana V, Pouchly V, Zadera A, Dlouhy I. In: The origins of high-entropy alloy contamination induced by mechanical alloying and sintering metals. 10; 2020. p. 1186.
[7] Otto F, Yang Y, Bei H, George EP. Relative effects of enthalpy and entropy on the phase stability of equiatomic high-entropy alloys. Acta Mater 2013;61:2628–38.
[8] Wu PH, Liu N, Yang W, Zhu ZX, Lu YP, Wang XJ. Microstructure and solidification behaviour of multicomponent CoCrCuxFeMoNi high-entropy alloys. Mater Sci Eng A 2015;642:142–9.
[9] Wu Z, Bei H, Otto F, Pharr GM, George EP. Recovery, recrystallization, grain growth and phase stability of a family of FCC-structured multi-component equiatomic solid solution alloys. Intermetallics 2014;46:131–40.
[10] Guo S, Ng C, Liu CT. Anomalous solidification microstructures in co-free AlxCrCuFeNi2 high-entropy alloys. J Alloys Compd 2013;554:77–81.
[11] Wang WR, Wang WL, Yeh JW. Phases, microstructure and mechanical properties of AlxCoCrFeNi high-entropy alloys at elevated temperatures. J Alloys Compd 2014;589:143–52.
[12] Jablonski PD, Licavoli JJ, Gao MC, Hawk JA. Manufacturing of high entropy alloys. JOM 2015;67(10):2278–87.
[13] Licavoli JJ, Gao MC, Sears JS, Jablonski PD, Hawk JA. Microstructure and mechanical behavior of high-entropy alloys. J Mater Eng Perform 2015;24(10):3685–98.
[14] Choi N, Lim KR, Na YS, Glatzel U, Park JH. Characterization of non-metallic inclusions and their influence on the mechanical properties of a FCC single-phase high-entropy alloy. J Alloys Compd 2018;763:546–77.
[15] MacDonald BE, Fu Z, Wang X, Li Z, Chen W, Zhou Y, Raabe D, Schoenung J, Hahn H, Lavernia EJ. Influence of phase decomposition on mechanical behavior of an equiatomic CoCuFeMnNi high entropy alloy. Acta Mater 2019;181:25–35.
[16] Miracle DB, Senkov ON. A critical review of high entropy alloys and related concepts. Acta Mater 2017;122:448–511.
[17] Choi N, Park N, Karasev AV, Jönsson PG, Park JH, Kim J-K. In: Influence of Manufacturing Conditions on Inclusion Characteristics and Mechanical Properties of FeCrNiMnCo Alloy Metals. 10; 2020. p. 1286.
[18] Tillmann W, Ulitzka T, Wojarski L, Manka M, Ulitzka H, Wagstyl D. Development of high entropy alloys for brazing applications. Weld World 2020;64:201–8.
[19] Hardwick L, Rodgers P, Pickering E, Goodall R. Development of a novel ni-based multi-principal element alloy filler metal, using an alternative melting point depressant. Metall Mater Trans A 2021;52A:2534–48.
[20] Luo D, Xiao Y, Hardwick L, Snell R, Way M, Morell XS, Livera F, Ludford N, Panwisawas C, Dong H, Goodall R. High entropy alloys as filler metals for joining. Entropy 2021;23:78.
[21] Bridges D, Zhang S, Lang S, Gao M, Yu Z, Feng Z, Hu A. Laser brazing of a nickel-based superalloy using a ni-mn-fe-co-cu high entropy alloy filler metal. Mater Lett 2018;215:11–4.
[22] Gao M. In: Development of new high-entropy alloys for brazing of Ni-base superalloys. Golden, CO: George S. Ansell Department of Metallurgical and Materials Engineering, Colorado School of Mines; 2017. p. 98.
[23] Gao M, Schneiderman B, Gilbert SM, Yu Z. Microstructural evolution and mechanical properties of Nickel-Base superalloy brazed joints using a MPCA filler. Metall Mater Trans A 2019;50:5117–27.
[24] Schneiderman B. Solidification mechanisms of a multi-principal-component alloy for filler applications. Golden, CO: Department of Metallurgical and Materials Engineering, Colorado School of Mines; 2020.
[25] Schneiderman B, DeNonno O, Klemm-Toole J, Yu Z. Ductile braze repairs for Ni-Base superalloys using novel MPEA filler. Weld J 2022;101(3):85s–95s.
[26] Inconel Alloy 600 Technical Brochure. Special Metals Corporation. 2008.
[27] Alloy IN-738 technical data, The International Nickel Company.
[28] Schneiderman B, Chuang AC, Kenesei P, Yu Z. In-situ synchrotron diffraction and modeling of non-equilibrium solidification of a MnFeCoNiCu alloy. Sci Rep 2021;11:5921.
[29] Gupta SK. Peak decomposition using Pearson type VII function. J Appl Cryst 1998;31:474–6.
[30] Toby BH, VonDreele RB. GSAS-II: the genesis of a modern open-source all purpose crystallography software package. J Appl Cryst 2013;46:544–9.
[31] Alcock CB, Itkin VP, Horrigan MK. Vapour pressure equations for the metallic elements: 298–2500K. Can Metall Quart 1984;23(3):309–13.
[32] Jain A, Ong SP, Hautier G, Chen W, Richards WD, Dacek S, Cholia S, Gunter D, Skinner D, Ceder G, Persson KA. Commentary: the materials project: a materials genome approach to accelerating materials innovation. APL Mater 2013;1(1).
[33] Ellingham HJT. Reducibility of oxides and sulphides in metallurgical processes. J Soc Chem Ind 1944;63(5):125–60.
[34] Gale WF, Butts DA. Overview: transient liquid phase bonding. Sci Technol Weld Join 2004;9(4):283–300.